Soil Dynamics and Earthquake Engineering 162 (2022) 107391

Contents lists available at ScienceDirect

Soil Dynamics and Earthquake Engineering

journal homepage: www.elsevier.com/locate/soildyn

# Residual drift risk of self-centering steel MRFs with novel steel column bases in near-fault regions

George S. Kamaris [a,*], Georgios S. Papavasileiou [b], Vasileios C. Kamperidis [c], George Vasdravellis [d]

[a] School of Civil Engineering and Built Environment, Liverpool John Moores University, Liverpool, L3 3AF, UK
[b] School of Computing, Engineering and Physical Sciences, Division of Engineering, University of the West of Scotland, Paisley, PA1 2BE, UK
[c] Department of Civil Engineering and Industrial Design, School of Engineering, Faculty of Science and Engineering, University of Liverpool, The Quadrangle, Brownlow Hill, Liverpool, L69 3GH, UK
[d] Institute for Infrastructure and Environment, Heriot-Watt University, Edinburgh, EH14 4AS, UK

ARTICLE INFO

*Keywords:*
Steel frames
Near-fault
Column base
Post-tensioned
Self-centering
Residual storey drifts
Seismic risk
Seismic hazard analysis

ABSTRACT

This paper evaluates the potential of novel steel column bases to reduce the residual drift risk of steel buildings located at near-fault regions when installed to post-tensioned self-centering moment-resisting frames (SC-MRFs). To this end, a prototype steel building is designed that consists of either conventional moment-resisting frames (MRFs) or SC-MRFs or SC-MRFs equipped with the novel steel column base (SC-MRF-CBs). The MRFs and SC-MRFs are used as benchmark frames. The frames are modelled in OpenSees where material and geometrical non-linearities are considered along with stiffness and strength degradation. A set of 91 near-fault ground motions with different pulse periods is used to perform incremental dynamic analysis (IDA), in which each ground motion is scaled appropriately until different residual storey drift limits are exceeded. The probability of exceedance of these limits is then computed as a function of the ground motion intensity and the period of the velocity pulse. Finally, the results of IDA are combined with probabilistic seismic hazard analysis models that account for near-fault directivity to evaluate and compare the residual drift risk of the frames used in this study. Results show that the predicted residual drift performance of the frames is influenced by the pulse period of the near-fault ground motions. The use of the novel steel column base significantly reduces the residual drift risk of the frames and the SC-MRF-CB exhibits the best residual drift performance. Finally, the paper highlights the effectiveness of combining post-tensioned beam-column connections with the novel steel column base, by showing that the SC-MRF-CB improves the residual drift performance of the MRF and SC-MRF by 80% and 50%, respectively.

## 1. Introduction

Earthquake ground motions that occur in the near-fault regions are often characterised by a long-duration and large-amplitude velocity pulse, observed at the beginning of the fault-normal (FN) ground velocity time-history. This type of pulse has a probability of occurrence which depends on the site-to-source geometry and a peculiar pulse period, which is a function of the earthquake magnitude [1,2]. These pulse-like near-fault ground motions are generated when the fault rupture propagates towards the site and the rupture velocity is close to the shear-wave velocity. This results to the constructive interference of the seismic wavefront and the arrival of the seismic energy from the rupture in the form of a large-amplitude pulse [3]. The seismic response of non-linear single-degree-of-freedom systems subjected to near-fault ground motions has been extensively investigated [ [4–7] and references therein]. Moreover, the seismic performance of yielding moment-resisting frames (MRFs) in the near-fault regions has been studied showing increased storey drifts [ [8–11] and references therein]. All the above studies concluded that near-fault ground motions have the potential to induce larger inelastic displacement demands compared to ordinary far-fault ground motions and to increase structural seismic risk.

The catastrophic potential and the increased seismic risk of near-fault ground motions has been pronounced by several recent earthquakes: e.g., the 1994 Northridge, California (M6.7); 1995 Kobe, Japan

* Corresponding author.
*E-mail address:* g.kamaris@ljmu.ac.uk (G.S. Kamaris).

https://doi.org/10.1016/j.soildyn.2022.107391
Received 14 April 2022; Received in revised form 6 June 2022; Accepted 9 June 2022
Available online 12 August 2022

(M6.9); 1999 Chi-Chi, Taiwan (M7.6); 2009 L'Aquila, Italy (M6.3); and 2016–17 Central Italy sequence (featuring events with magnitude ranging between 5.5 and 6.5). These seismic events highlighted the limitations of conventional seismic-resistant systems, that are designed to exhibit significant inelastic deformations in their structural members under strong earthquakes. Inelastic deformations can result to severe damage in the structural members and appreciable residual storey drifts, leading to high repair costs and disruption of the building occupancy. Residual drifts are recognised as an important seismic performance index which is directly related to the probability of demolition of a building. McCormick et al. [12] concluded that it was in general less costly to demolish and rebuild a steel building in Japan than to repair it when the values of residual storey drifts were larger than 0.5%. It should be noted that residual displacements show significant record-to-record variability compared to peak displacements [13]. Thus, designing conventional yielding structures to be reparable in the aftermath of strong earthquakes involves significant uncertainty. In addition, the potential of near-fault ground motions to induce large residual storey drifts [14] is not considered by current seismic design codes [15].

To address the socio-economic risks caused by strong earthquakes, the self-centering MRFs (SC-MRFs) with post-tensioned (PT) beam-column connections were developed [16–26]. This type of frames exhibits softening force-drift behaviour and eliminates beam plastic deformations due to gap opening developed in beam-column interfaces and elastic PT strands or bars which clamp beams to the columns and provide self-centering capability. Energy dissipation devices are used in the PT connections of SC-MRFs, which are activated when gaps open. These devices can be easily replaced if damaged improving building's resilience [16–26]. Seismic design procedures for SC-MRFs are provided in [27,28].

However, SC-MRFs with conventional column bases develop plastic hinges at their column bases and thus cannot fully avoid structural damage and residual drifts [29–31]. To address this issue, SC-MRFs with self-centering column bases with repairable energy dissipation devices (SC-MRF-CBs) were proposed [29–38]. SC-MRF-CBs can avoid damage at their column bases and, thus, eliminate residual drifts. Few studies investigated the effectiveness of SC-MRF-CBs to increase seismic resilience. Freddi et al. [31] have found that these systems do not exhibit yielding in the first storey columns and eliminate the first storey residual drift. Moreover, Kamperidis et al. [30] have shown that these systems significantly improve the seismic performance of their correspondent SC-MRFs. Finally, Kamperidis et al. [38] studied the collapse performance of SC-MRF-CBs subjected to far-fault ground motions and found that the SC-MRF-CBs have significantly larger collapse resistance than that of the SC-MRFs.

All the abovementioned studies on SC-MRF-CBs have focused on their seismic performance when subjected to far-fault ground motions. In this paper, the seismic behaviour of SC-MRF-CBs subjected to near-fault ground motions is studied for the first time. Moreover, the potential of using SC-MRF-CBs to reduce the probability of demolition due to large residual storey drifts of steel buildings in near-fault regions has never been investigated. To this end, a rigorous and novel methodology based on the theorem of total probability is proposed for the calculation of the residual drift risk of steel buildings located in near-fault regions. A prototype steel building is designed that consists of either conventional MRFs or SC-MRFs or SC-MRF-CBs. The novel steel column base proposed by Kamperidis et al. [30] is used in this study. The frames are modelled in OpenSees [39] where material and geometrical non-linearities are considered as well as stiffness and strength degradation. A set of 91 near-fault ground motions with different pulse periods is used to perform incremental dynamic analysis (IDA) [40]. The probability of exceedance of different residual storey drift limits is then calculated as a function of the ground motion intensity and the period of the velocity pulse. Finally, the results of IDA are combined with probabilistic seismic hazard analysis (PSHA) models that take into account near-fault directivity to evaluate and compare the residual drift risk of the three seismic-resistant frames used in this study.

## 2. Novel steel column base

Fig. 1(a) depicts the configuration of the novel steel column base, while its theoretical moment-rotation ($M$-$\theta$) behaviour is shown in Fig. 1 (b). The column base comprises 4 high-strength PT tendons and 8 web hourglass shape pins (WHPs). The column is welded on a strong steel plate (anchor stand), that is welded on a concrete filled steel tube (CFT) which serves as the column foot. The PT tendons are anchored to the bottom of the concrete foundation and the anchor stand, as shown in Fig. 1(a) (Detail 1). The PT tendons clamp the CFT to a base plate to provide self-centering capability, moment resistance and rotational stiffness. Moreover, the tendons exert their PT forces only to the CFT, because they are placed within the concrete foundation. In this way, the PT forces of the tendons are resisted by the CFT instead of the column and the latter avoids any undesirable axial shortening due to the PT forces. Furthermore, the column can achieve better rotation capacity as it does not receive the large PT forces. The use of the CFT as a column foot helps the column base to form a strong rocking interface and thus enhance its self-centering and low-damage capability.

The anchor stand offers flexibility in the arrangement of the tendons, and thus, in the selection of their lever arms (Fig. 1(a)). The anchor stand is reinforced with stiffeners to avoid excessive bending due to the large PT forces, protecting the tendons from loss of post-tensioning. The WHPs are inserted in aligned holes drilled on supporting plates welded on the base plate and on web plates welded on the four sides of the CFT (Fig. 1 (a)). The WHPs possess high fracture capacity due to their optimised shape and provide enhanced energy dissipation via inelastic bending [41].

The shear resistance of the column base is achieved through friction in the rocking interface and through steel elements (shear bumpers) bolted on the base plate against the four sides of the CFT (Detail 2 in Fig. 1(a)). These shear bumpers are detailed to avoid interlocking during the rocking of the CFT.

## 3. Prototype building and design of the seismic-resistant frames

Fig. 2 depicts the plan view of the 5-bay by 3-bay five-storey prototype steel building [29] utilised herein. The building has at its perimeter two identical braced frames in the $Y$ direction and two identical seismic-resistant frames in the $X$ direction. The building has ductile non-structural elements and thus the maximum interstorey drift ratio must be less than 0.75% under the frequent occurred earthquake in accordance with EC8 [15]. A type 1 EC8 design spectrum [15] with peak ground acceleration equal to 0.35 g and ground type B was used for the design of the frames under the design basis earthquake.

Only the seismic-resistant frame of Elevation A of the prototype building is investigated (Fig. 2(b)). This frame was designed either as (a) an MRF or (b) an SC-MRF or (c) an SC-MRF-CB with the novel steel column base [30]. The MRF, SC-MRF and SC-MRF-CB have the same beams and columns. The design characteristics of the members and beam-column connections of the MRF and SC-MRF are the same as those of the frames in [14]. Fig. 3(a) shows the bottom-left part of an SC-MRF-CB in Elevation A of the prototype building. The configurations of an external and internal (central) PT beam-column connection of the frames are shown in Fig. 3(a). Fig. 3(b) depicts a close-up view and the notation of an external PT beam-column connection. The design procedure proposed in [30] was utilised for the design of the novel steel column bases of the SC-MRF-CB. The design characteristics of the SC-MRF-CB are presented in Table 1. The notation used in Table 1 is described in Fig. 3(c). For the WHPs of the column bases, duplex stainless steel is used with the following properties [41]: yield stress of 543 MPa; ultimate stress of 778 MPa; elongation at fracture equal to 34.25%; and modulus of elasticity equal to 227.848 GPa. The material for the multi-wire tendons of the novel steel column base is the

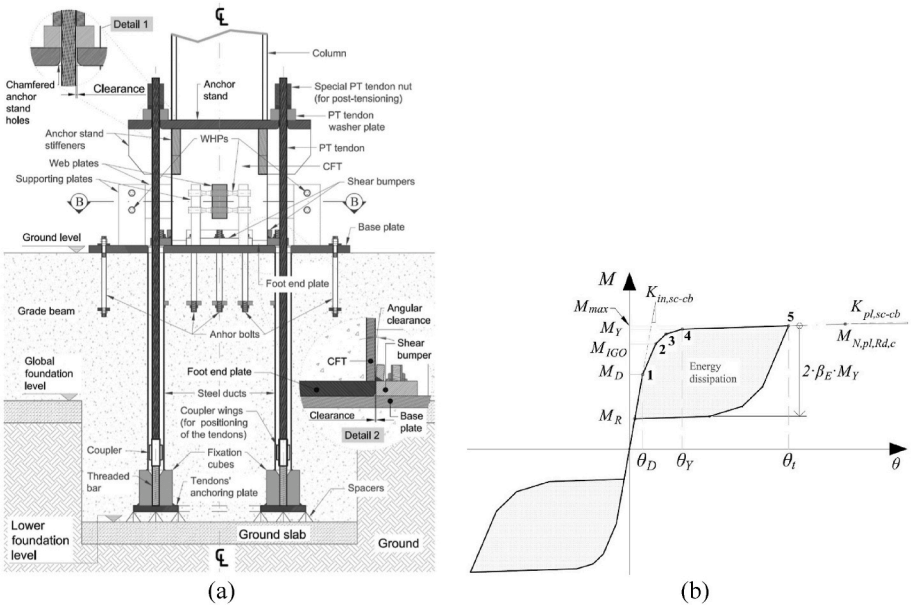


**Fig. 1.** Novel steel column base: (a) configuration and notation; (b) theoretical *M-θ* behaviour [38].

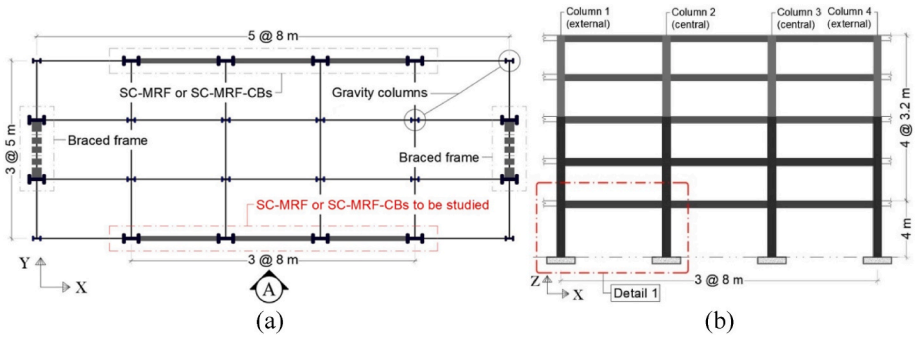


**Fig. 2.** (a) Plan view; and (b) Elevation A of the prototype building.

low-relaxation Grade 270 steel material of ASTM A416 [42].

## 4. Non-linear models of the seismic-resistant frames

The OpenSees software [39] was used for the modelling of the seismic-resistant frames of this work. The PT beam-column connections of the SC-MRF and SC-MRF-CB are modelled as in [14]. The columns and the reinforced lengths of the beams are modelled with beam-column fibre elements with bi-linear elastoplastic stress-strain behaviour. Force-based beam-column fibre elements with end hinges [43] are utilised to model the un-reinforced lengths of the beams. The modified Ibarra-Krawinkler model [44] is used to model the stress-strain cyclic behaviour of the fibres. This model is used because it captures the strength and stiffness deterioration that results from the beam local buckling observed after the end of the beam flange reinforcing plates. The use of fibre elements results in reduction of the bending strength of the beam-column elements due to the variable axial-moment interaction [45] that is not considered by the Ibarra-Krawinkler model. The panel zones are modelled using the model proposed in [46]. The gravity columns associated with the frames are modelled as lean-on columns to take into account the P-Δ effects. Diaphragm action is modelled with truss elements connecting the lean-on columns nodes to nodes defined along the length of the beams at the points where secondary beams are placed. These trusses have stiffness of 100 times the axial beam stiffness.

The model developed by Kamperidis et al. [30] is used for the novel steel column bases of the SC-MRF-CB. This model is shown in Fig. 4. The rocking interface, CFT and anchor stand are modelled by rigid elastic beam-column elements. Three zero-length translational contact springs placed at equal distances along the left and right half-depth-part of the CFT cross-section are used to simulate rocking. A zero-length hysteretic spring that follows a smooth Giuffre-Menegotto-Pinto hysteretic rule with isotropic hardening is used to model each WHP group. This spring is placed at the geometric centre of each group. The tendons are modelled as truss elements with bilinear elastoplastic hysteresis.

Rigid and full strength connections are assumed for the MRF, while beams are modelled as elastic elements with zero length rotational springs at their ends that exhibit strength and stiffness degradation [44]. The columns and panel zones of the MRF are modelled as described above for the SC-MRF. Finally, the fundamental period, $T_1$, obtained from the OpenSees models is 1.180 s for the MRF, 0.944 s for the SC-MRF and 0.881 s for the SC-MRF-CB.

## 5. Ground motions

A set of 91 near-fault ground motions is employed as input for the non-linear dynamic time history analyses. This set was compiled by Baker [47] from the PEER Next Generation Attenuation (NGA) database [48] employing wavelet analysis to detect and determine the pulse period, $T_p$. This set only includes FN ground motions having a minimum peak ground velocity of 30 cm/s. Ground motions were recorded from

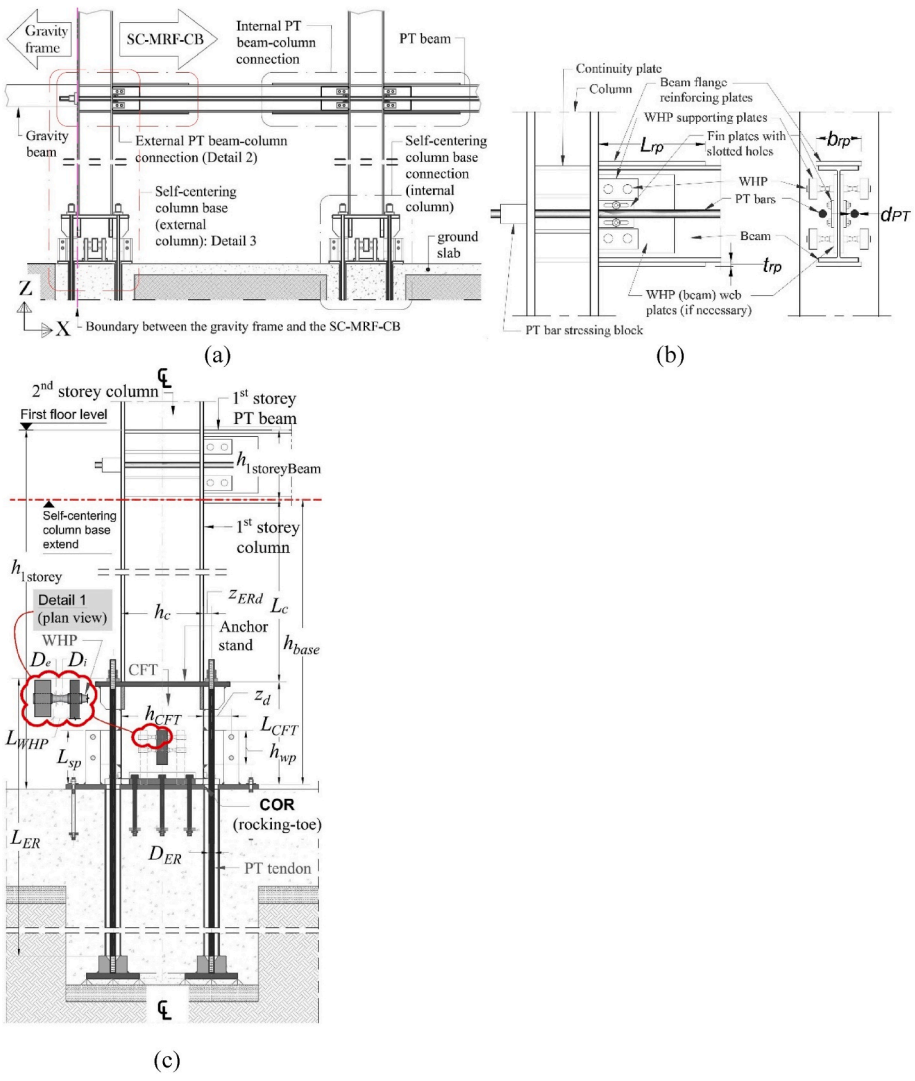


**Fig. 3.** Close-up view of: (a) the bottom-left part of the SC-MRF-CB in Elevation A of the prototype building (Detail 1 in Fig. 2(a)); (b) external PT beam-column connection with its notation (Detail 2 in Fig. 3(a)); and (c) configuration (Detail 3 in Fig. 3(a)) and notation [38].

**Table 1**
Key design characteristics of the novel steel column base of the SC-MRF-CB.

| $L_{WHP}$ (m) | $D_e$ (m) | $D_i$ (m) | $F_{y,WHP,i}$ (kN) | $K_{fe}$ (MN/m) | $L_{sp}$ (m) | $h_{wp}$ (m) | $L_{ER}$ (m) | $D_{ER}$ (m) | $z_d$ (m) | $z_{ER,d}$ (m) | $L_{CFT}$ (m) | $T_{pt}$ (kN) |
|---|---|---|---|---|---|---|---|---|---|---|---|---|
| 0.06 | 0.04 | 0.02 | 125.24 | 251.67 | 0.31 | 0.19 | 8.70 | 0.02 | 0.34 | 0.50 | 0.91 | 212.51 |

earthquakes with moment magnitudes, $M$, varying from 5.0 to 7.6 and include pulse periods that range between 0.4 and 12.9 s. Although all the records exhibit velocity pulses, site-to-source distance was not considered as a selection criterion and varies from 0.10 to 102 km. Therefore, some of the observed pulses were probably caused by other geological mechanisms, such as the sedimentary basin effect. A complete list of the near-fault pulse-like ground motions used in this work can be found in [47].

In this work, the residual drift performance of the frames depends on the probability of occurrence or not of a pulse-like ground motion and is computed through the theorem of total probability. Thus, a second set of far-fault records is necessary for the determination of the probability of exceedance of certain limits of residual storey drifts for sites that are not affected by forward directivity. Similarly to previous studies [11,14], the set of far-fault ground motions used herein is based on the FEMA P695 [49] far-fault ground motion set. This set includes 22 record pairs, each with two horizontal components for a total of 44 ground motions. These ground motions are recorded at sites located greater than or equal to 10 km from fault rupture. Event magnitudes vary from $M$ 6.5 to $M$ 7.6 with an average magnitude of $M$ 7.0. It is worth noting that the ground motion records in FEMA P695 [49] were selected without consideration of the spectral shape. In fact, the FEMA P695 [49] far-fault ground motion set comprises records that are structure type and site hazard independent.

## 6. Residual drift assessment

Significant economic losses were reported in recent earthquake events, because structures experienced excessive residual drifts, $\theta_{s,res}$, even if they were not severely damaged or partially collapsed, and they had to be demolished [13]. The assessment of $\theta_{s,res}$ is very important for deciding if it is technically and economically feasible to repair or retrofit a structure that has been damaged due to an earthquake. For this reason, an evaluation of the residual drift performance of the frames considered

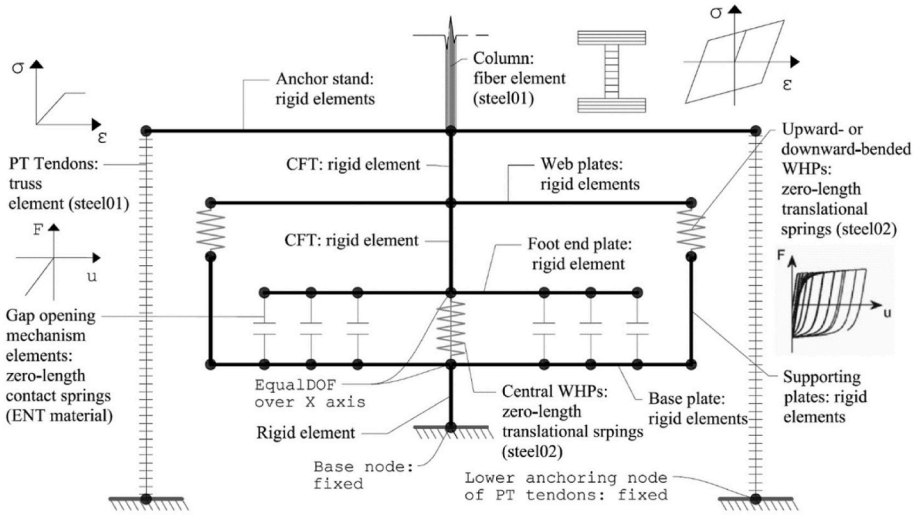


**Fig. 4.** Non-linear model of the novel steel column base.

in this work is performed. McCormick et al. [12] have suggested a value of 0.5% as a limit of the permissible $\theta_{s,res}$, which is adopted here. Furthermore, two additional values of permissible $\theta_{s,res}$ are assumed (i.e., 0.2% and 1.0%) to investigate the effect of this parameter in the residual drift performance of the frames. These two limits are based on the recommendation of FEMA 356 [50] for the immediate occupancy and life safety limit states, respectively. The limit value proposed by McCormick et al. [12] is very similar to the value adopted by FEMA 356 [50] for the reparability limit state, which is 0.4%.

The residual drift risk of each frame is evaluated through IDA [36], i.e. the model of the frame is subjected to a specific ground motion that is increasingly scaled until a prescribed value of $\theta_{s,res}$ (i.e., $\theta_{lim}$) is exceeded. The spectral acceleration at the fundamental period, $T_1$, of the frame, $S_a(T_1)$, is used as the seismic intensity measure (IM) and $\theta_{s,res}$ is the response parameter that is monitored. Fig. 5(a) shows the IDA curves for the SC-MRF-CB for the set of the far-fault ground motions. For each seismic-resistant frame and ground motion, the value of $S_a(T_1)$ at which the $\theta_{lim}$ value is reached was obtained. Each dynamic analysis was extended well beyond the actual earthquake time to allow for damped free vibration decay and accurate computation of $\theta_{s,res}$.

Using the results of the IDAs, a residual drift fragility curve is generated that gives the probability of exceedance of $\theta_{s,res}$. This is done by fitting a lognormal cumulative distribution function to the $S_a(T_1)$ values that correspond to the $\theta_{s,res}$ values of each frame. The median value and the lognormal standard deviation of the ground motion intensities at which $\theta_{s,res}$ is exceeded in IDA define this distribution. The fragility curve for permissible $\theta_{s,res}$ equal to 0.5% resulted for the SC-MRF-CB is shown in Fig. 5(b) with a solid line together with the numerical results obtained from the non-linear dynamic analyses.

The lognormal standard deviation, $\beta$, influences the shape of the fragility curve and reflects the level of uncertainty in the analyses results. Two sources of uncertainty in quantifying the residual drift risk of the frames are considered herein: aleatory sources and epistemic. The aleatory or record-to-record uncertainty ($\beta_{RTR}$) reflects the variability in the response of the structures due to the random nature of ground motions. The epistemic or modelling uncertainty ($\beta_{modelling}$) is mainly due to lack of knowledge about the structure's real model and real element properties. It is associated with non-linear modelling, based on the evaluation of the accuracy and robustness of the non-linear models used and their ability to represent the true physical properties and the seismic response of structures.

In order to combine the contributions of record-to-record and modelling uncertainties, the mean estimates approach is used [51]. According to this approach, the record-to-record uncertainty, $\beta_{RTR}$, and the modelling uncertainty, $\beta_{modelling}$, are assumed to be lognormally distributed and independent, such that the total uncertainty, $\beta_{Total}$, is given by:

$$\beta_{Total} = \sqrt{\beta_{RTR}^2 + \beta_{modelling}^2} \quad (1)$$

Therefore, the median is unchanged when modelling uncertainties are incorporated, but the standard deviation increases as shown in Fig. 5(b). The value of $\beta_{Total}$ is taken as 0.80 in line with previous studies [11,

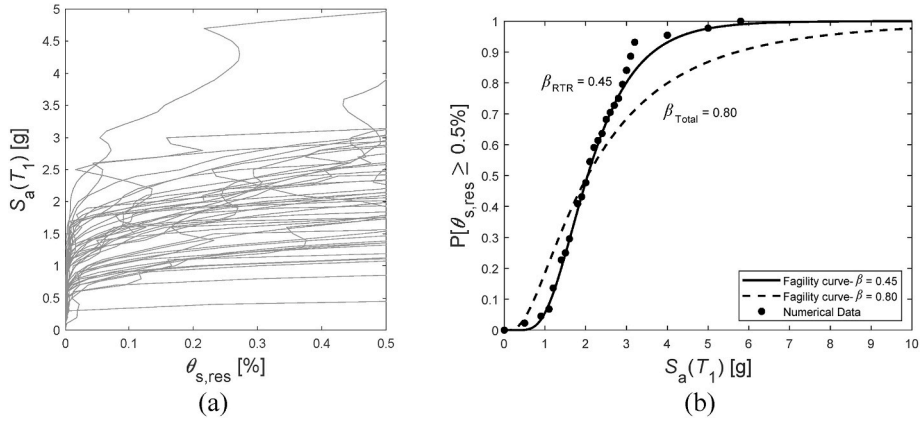


**Fig. 5.** (a) IDA curves of the SC-MRF-CB and (b) Corresponding fragility curve.

14]. It should be noted that this choice may lead to slightly conservative absolute values [11,14]. However, different values of $\beta_{\text{Total}}$ would change the absolute value of the residual drift evaluations but would not significantly affect the relative comparison among the three frames.

The procedure used for the evaluation of the residual drift risk due to the near-fault ground motions is properly modified to account for the effect of the pulse period of the record, $T_p$, and is based on the approach proposed by Champion and Liel [11]. This methodology is described in the following sections.

## 7. Effect of the pulse period on residual drift performance

Past research [8,11,14] has shown that the ratio of the pulse period, $T_p$, of the near-fault ground motions over $T_1$ has a critical effect on seismic response of structures. To demonstrate this effect on the frames of this work, the $S_a(T_1)$ values that exceed the permissible $\theta_{s,res} = 0.5\%$ (residual drift $S_a(T_1)$) of the SCMRF-CB obtained from the IDA curves (Fig. 5(a)) are plotted versus the ratio $T_p/T_1$ and depicted in Fig. 6 as individual points. Moreover, the moving average of the numerical data is computed by averaging the point of interest with the five previous and subsequent data points. This procedure is followed to fit the data points with a trend-line that shows the behaviour of the residual drift $S_a(T_1)$ values as a function of $T_p/T_1$.

The shape of the moving average curve illustrates the influence of $T_p$ on the residual drift $S_a(T_1)$. It is observed from Fig. 6 that the maximum values of residual drift $S_a(T_1)$ can be found in the region of the moving average curve where the $T_1$ of the SCMRF-CB is approximately equal to the $T_p$ of the record, i.e., $T_p/T_1 \approx 1$. This result indicates that the frame is less vulnerable in exhibiting residual drift when its fundamental period is very close to the $T_p$ of the excitation. This observation is inconsistent with the elastic seismic response of structures, because their largest displacement demand is observed when the period of the excitation is very close to $T_1$. However, the residual drift performance of a structure is related to large plastic deformations, which lead to a reduction of the structural stiffness. As a result, the effective period of the structure is significantly elongated and is different than $T_1$. Thus, residual drift $S_a(T_1)$ is larger in the region where $T_p/T_1 \approx 1$ as it is affected by the real elongated period of the structure, which is different than $T_p$. Moreover, the ground motions with pulse period $T_p > T_1$ are the most damaging, giving very low values for the residual drift $S_a(T_1)$. This is due to the effective lengthened period of the frame that tends to coincide with the pulse period of the excitation. In the region of $T_p < T_1$, the residual drift $S_a(T_1)$ of the frame tends to decrease which can be attributed to the fact that shorter pulse periods are exciting the higher modes of the structure.

To obtain the effect of the frame type on the residual drift $S_a(T_1)$ as a function of the pulse period of the near-fault records, the moving average curves for all the frames of this work are generated and shown in Fig. 7. To allow comparison between the frames having different $T_1$ values, the residual drift $S_a(T_1)$ values of each moving average curve are normalised by the median residual drift $S_a(T_1)$ of all the near-field records. Comparing the moving average curves of all the frames, it is apparent from Fig. 7 that all the frames follow the same overall trend observed in Fig. 6. This can be explained by the fact that all the frames were designed to have similar base shear and ductility. Thus, their residual drift behaviour depends on the pulse period by the same manner.

## 8. Fragility functions incorporating the effect of near-fault directivity

As shown in the previous section, near-fault directivity has an impact on residual drift $S_a(T_1)$ of structures, so it should be considered in their residual drift risk assessment. The residual drift performance of structures depends not only on $S_a(T_1)$, but also whether a ground motion record exhibits a velocity pulse and the corresponding pulse period, $T_p$ (see Figs. 6 and 7). To incorporate this effect in the residual drift fragility functions, the theorem of total probability is used to compute the probability of exceedance of $\theta_{s,res}$ equal to $\theta_{lim}$, $P[\theta_{s,res} \geq \theta_{lim}|S_a = x]$, for a given $S_a(T_1)$ value of $x$. This probability is the fragility function of each frame [11,14] and can be expressed as:

$$P\left[\theta_{s,res} \geq \theta_{lim}\middle|S_a = x\right] = P\left[\theta_{s,res} \geq \theta_{lim}\middle|S_a = x, \quad \text{Pulse}\right] \cdot P[\text{Pulse}|S_a = x] + P\left[\theta_{s,res} \geq \theta_{lim}\middle|S_a = x, \text{No} \quad \text{Pulse}\right] \cdot P[\text{No} \quad \text{Pulse}|S_a = x] \tag{2}$$

where $P[\theta_{s,res} \geq \theta_{lim}|S_a = x, \text{Pulse}]$ is the probability of exceedance of $\theta_{s,res}$ equal to $\theta_{lim}$ for near-fault, pulse-like ground motions; $P[\theta_{s,res} \geq \theta_{lim}|S_a = x, \text{No Pulse}]$ is the probability of exceedance of $\theta_{s,res}$ equal to $\theta_{lim}$ for far-fault ground motions; $P[\text{Pulse}|S_a = x]$ is the probability that a ground motion record exhibits a velocity pulse; and $P[\text{No Pulse}|S_a = x]$ is the probability that a ground motion record does not exhibit a velocity pulse.

The term $P[\theta_{s,res} \geq \theta_{lim}|S_a = x, \text{No Pulse}]$ is calculated from the fragility curves constructed for the far-fault ground motions. The probability of exceedance of $\theta_{s,res}$ equal to $\theta_{lim}$ when a pulse occurs, $P[\theta_{s,res} \geq \theta_{lim}|S_a = x, \text{Pulse}]$, depends on the pulse period and the likelihood of different pulse periods occurring, $P[T_p = t_i|S_a = x, \text{Pulse}]$:

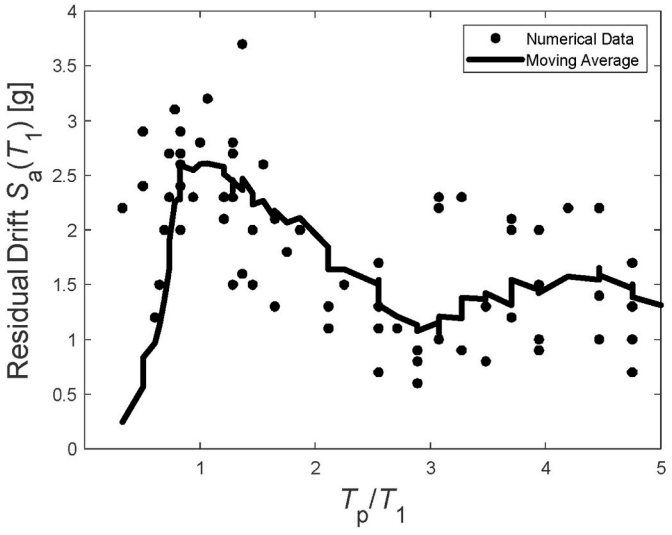


**Fig. 6.** Residual drift $S_a(T_1)$ of the SC-MRF-CB versus the $T_p/T_1$ ratio together with the moving average curve.

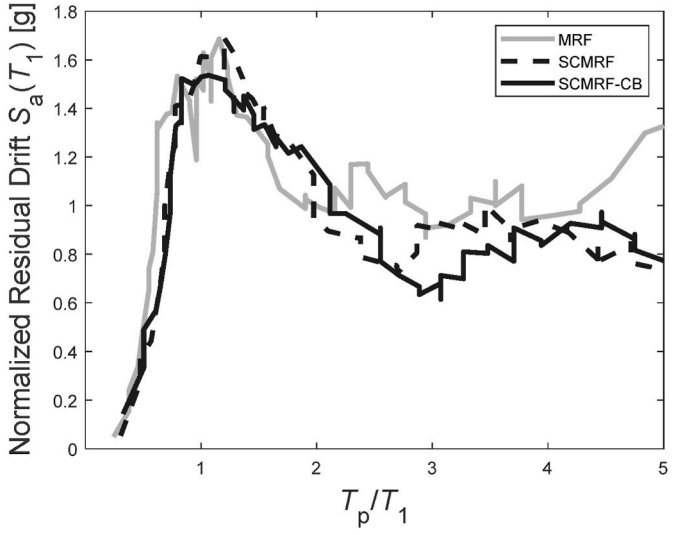


**Fig. 7.** Moving average curves representing normalised residual drift $S_a(T_1)$ as a function of $T_p/T_1$ for the frames of this study.

$$P\left[\theta_{s,res} \geq \theta_{\lim} \middle| S_a = x,\ \text{Pulse}\right] = \sum_{i=1}^{All T_p} P\left[\theta_{s,res} \geq \theta_{\lim} \middle| T_p = t_i, S_a = x,\ \text{Pulse}\right] \cdot P\left[T_p = t_i \middle| S_a = x,\ \text{Pulse}\right] \tag{3}$$

The probability of exceedance of $\theta_{s,res}$ equal to $\theta_{lim}$ for a given pulse period $T_p$ value, $P[\theta_{s,res} \geq \theta_{lim}|T_p = t_i, S_a = x, \text{Pulse}]$, is determined by the moving average curve constructed for each frame. The moving average represents the median residual drift $S_a(T_1)$ as a function of $T_p$. For any value of $T_p$ and $S_a(T_1)$, $P[\theta_{s,res} \geq \theta_{lim}|T_p = t_i, S_a = x, \text{Pulse}]$ is calculated by assuming a lognormal distribution with a median equal to the value of $S_a(T_1)$ of the moving average curve for the given $T_p$ and a standard deviation $\beta_{Total} = 0.8$.

The remaining parts of Equations (2) and (3) are calculated with the aid of PSHA, which provides the mean annual frequency, $\lambda$, of exceeding an IM level, $x$. Conventional far-field PSHA provides $\lambda$ according to the following equation:

$$\lambda_{IM>x} = \sum_{i=1}^{N} \nu_i \int_m \int_r P[IM > x|m, r] f_{M,R}(m, r) dm dr \tag{4}$$

where $\nu_i$ is the mean annual rate of earthquakes occurrence on a nearby fault $i$, $N$ is the total number of faults, $M$ is the moment magnitude, $R$ is the source-to-site distance and $f_{M,R}$ is the joint probability density function of $M$ and $R$. The term $P[IM > x|m, r]$ is the probability that the ground motion intensity exceeds a specific value, $x$, given an earthquake of magnitude $m$ at distance $r$, which can be obtained through ground motion prediction equations. Different IMs can be used in these equations, in this work $S_a(T_1)$ is adopted.

PSHA has been modified to account for near-source conditions, i.e., Near-source Probabilistic Seismic Hazard Analysis (NS-PSHA) [1,52,53]. According to this methodology, Equation (4) is adjusted to account for the potential near-source directivity through the term $Z$:

$$\lambda_{IM>x} = \sum_{i=1}^{N} \nu_i \int_m \int_r \int_z P[IM > x|m, r, z] f_{M,R,Z}(m, r, z) dm dr dz \tag{5}$$

where $Z$ defines the site-to-source geometry and $f_{M,R,Z}$ is the joint probability density function of $M$, $R$ and $Z$. The term $P[IM > x|m, r, z]$ is the probability that a specific ground motion intensity value is exceeded, for a given earthquake of magnitude $m$ at distance $r$ and site-to-source geometry $z$. This probability depends on the probability of pulse occurrence, the distribution of possible pulse periods and the peculiar spectral shape caused by the pulse. The probability of pulse occurrence is a function of site-to-source geometry and decreases with distance from the fault and for shorter fault rupture lengths [1,53]. The pulse period distribution is a function of earthquake magnitude, with larger magnitude events usually causing longer pulse periods [53,54].

When the NS-PSHA has been conducted for a given IM level, the term $P[\text{Pulse}|S_a = x]$, can be calculated by the following equation:

$$P[\text{Pulse}|S_a = x] = \frac{\lambda_{S_a=x,\text{Pulse}}}{\lambda_{S_a=x,\text{Total}}} \tag{6}$$

where $\lambda_{S_a=x,\text{Pulse}}$ is the mean annual frequency of $S_a = x$ when only near-fault, pulse-like ground motions are considered and $\lambda_{S_a=x,\text{Total}}$ is the mean annual frequency of $S_a = x$ when both near-fault and far-fault ground motions occur. Note that NS-PSHA is computed here as $\lambda_{S_a=x}$ rather than $\lambda_{S_a>x}$ to allow for combination with the residual drift fragility curves. The hazard disaggregation of Eq. (6) is required for each spectral acceleration level of interest (from the fragility). A similar disaggregation procedure is also used to identify the contribution of each pulse period, $t_i$, to each spectral value, i.e., $P[T_p = t_1|S_a = x, \text{Pulse}]$. Finally, the term $P[No\ \text{Pulse}|S_a = x]$ is determined by the following equation:

$$P[\text{No Pulse}|S_a = x] = 1 - P[\text{Pulse}|S_a = x] \tag{7}$$

In this paper, a fixed (characteristic) $M$ 7 strike-slip (SS) fault is used to compare the residual drift risk of the three seismic-resistant frames. Based on the median Wells and Coppersmith magnitude-scaling relation [55], the length of this fault is equal to 42 km. The mean annual rate of earthquake occurrence on the fault is assumed to be 0.05 and the location of earthquake epicentres is uniformly distributed along the fault. Moreover, as shown in Fig. 8(a), six sites with site-to-source distances equal to 5, 10 and 15 km at the end ("End-of-Fault" sites) and midpoint ("Midfault" sites) of the fault line are considered in this study.

The model of Iervolino and Cornell [1] is used to compute the probability of the pulse occurrence. In the case of a SS rupture, this probability depends on the rupture-to-site distance, $R$, the distance from the epicentre to the site measured along the rupture direction, $s$, and the angle between the fault strike and the path from the epicentre to the site, $\theta$. The pulse period prediction is based on the empirical model in [2]. Finally, NS-PSHA results are shown in Fig. 8(b) for $T_1 = 0.944$ $s$. Fig. 8(c) and (d) provide disaggregated hazard results in terms of $P[\text{Pulse}|S_a = x]$ and $P[T_p = t_i|S_a = x, \text{Pulse}]$ respectively (the latter refer to $S_a = 1$ g as an example).

## 9. Residual drift risk of the frames in the near-source

Using the methodology of section 8, the fragility curves that give the probability of exceedance of $\theta_{s,res}$ equal to 0.5% for the case study of midfault sites at 15 km, are constructed for of all the frames and shown in Fig. 9(a). The fragility curves indicate that the frame equipped with the novel steel column bases has the best residual drift performance. The SC-MRF-CB exhibits the least probabilities of exceedance of the specified value of $\theta_{s,res}$, since its fragility curve is clearly shifted to the right of the fragility curves of all the other frames. Fig. 9(b) depicts the fragility curves constructed for the SC-MRF-CB when located at the midfault sites for site-to-source distances equal to 5, 10 and 15 km. It is observed that the probability of exceedance of $\theta_{s,res}$ equal to 0.5% is reduced with distance from the fault, because the likelihood that a pulse occurs, $P[\text{Pulse}|S_a = x]$, decreases with distance and that affects the first part of Equation (2).

In addition, the probability of exceedance of $\theta_{s,res}$ equal to 0.5% in 50 years, i.e., the residual drift risk of the frames, is computed at the midfault and end-of-fault sites, for site-to-source distances equal to 5, 10 and 15 km. To do so, a Poisson distribution of the earthquake occurrences is used, which is given by the following equation:

$$P\left[\theta_{s,res} \geq \theta_{\lim} in\ 50\ years\right] = 1 - e^{-\nu t} \tag{8}$$

where $t$ is the time in years and $\nu$ is the mean annual frequency of exceedance of a specified value of $\theta_{s,res}$, determined by integrating the residual drift probability distribution, i.e., the fragility curve of each frame, with the rate of exceedance for each spectral acceleration and site of interest. The results are listed in Table 2.

Increased residual drift risk at sites closer to the fault is observed from the results of Table 2. The probability of exceedance of the specified limit of $\theta_{s,res}$ in 50 years of the frames located at 10 km distant sites is 1.4–1.7 higher than that when they are at distance 15 km away from the fault, for the midfault sites. When the site-to-source distance is reduced from 15 to 5 km the probability of the frames exceeding the specified limit of $\theta_{s,res}$ is increased by a factor ranging from 2.2 to 3.3 for the midfault sites. Similar results are observed for the end-of-fault sites. Moreover, the residual drift risk of the frames is not as largely affected by the relative position of the site to the fault axis as it is by the distance to the fault. However, slightly larger values of the probability of exceedance of $\theta_{s,res}$ equal to 0.5% are found at the end-of-fault sites.

The results in Table 2 indicate that the SC-MRF-CB has approximately 63%, 71% and 76% less probability of exceeding $\theta_{s,res}$ equal to 0.5% in 50 years than that of the MRF for site-to-source distances equal to 5, 10 and 15 km, respectively, at the midfault sites. Moreover, the SC-MRF-CB has 18%, 21% and 23% reduced probability of exceeding $\theta_{s,res}$

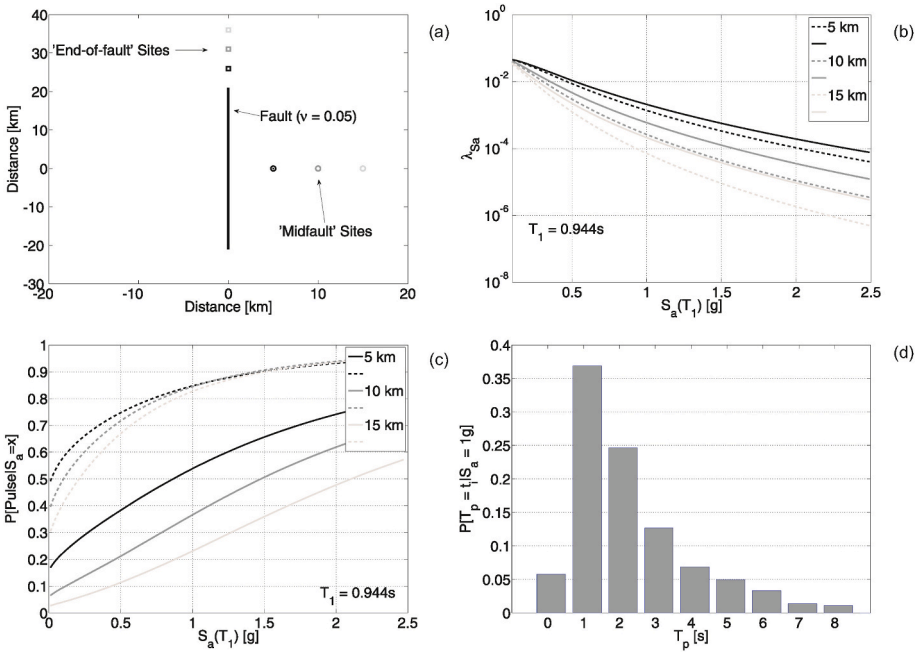


**Fig. 8.** Representative near-fault sites considered in this study, showing (a) site location and (b) seismic hazard curves for the "End-of-Fault" (solid lines) and "Midfault" (dashed lines) sites with varying site-to-source distances. Hazard disaggregation results show (c) the probability of pulse occurrence for the different sites at $S_a(T_1 = 0.944$ s) and (d) a typical pulse period distribution for one hazard level, $S_a(T_1) = 1$ g, at the 5 km "Midfault" site.

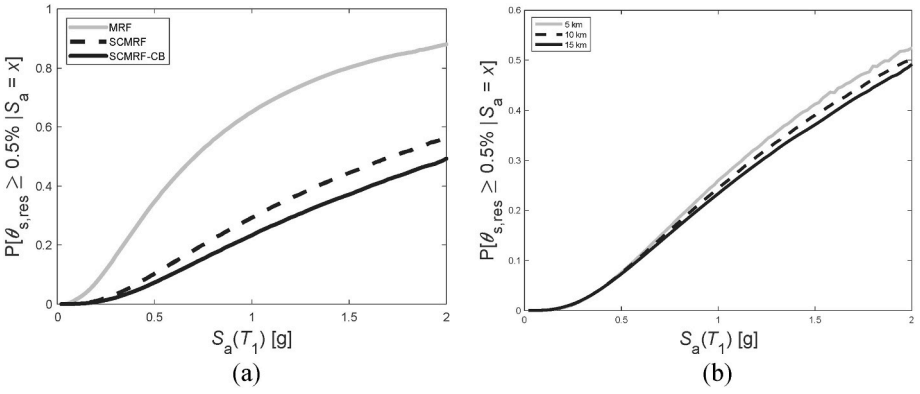


**Fig. 9.** Residual drift fragility curves for (a) the three frames located at midfault sites for site-to-source distance equal to 15 km and (b) the SC-MRF-CB at three different midfault sites.

**Table 2**
Probability of exceedance of $\theta_{s,res}$ equal to 0.5% in 50 years.

| Frame | P[$\theta_{s,res} \geq$ 0.5% in 50 yrs] | | | | | |
|---|---|---|---|---|---|---|
| | Midfault sites | | | End-of-fault sites | | |
| | 5 km | 10 km | 15 km | 5 km | 10 km | 15 km |
| MRF | 36.8% | 23.9% | 16.8% | 37.5% | 24.7% | 17.6% |
| SC-MRF | 16.5% | 8.7% | 5.4% | 17.0% | 9.1% | 5.7% |
| SC-MRF-CB | 13.5% | 6.8% | 4.1% | 14.0% | 7.2% | 4.4% |

equal to 0.5% in 50 years than that of the SC-MRF for site-to-source distances equal to 5, 10 and 15 km, respectively, at the midfault sites. A similar trend is observed at the end-of-fault sites for all the frames. Therefore, the SC-MRF-CB has the best residual drift performance among the three frames with probabilities of exceedance of $\theta_{s,res}$ equal to 0.5% in 50 years significantly lower than those of both the MRF and SC-MRF. It should be also noted that the decrease of the residual drift achieved by the SC-MRF-CB compared to the SC-MRF refers mainly to the first storey at the column bases. This is because the beams of the SC-MRF do not experience residual drifts due to the PT connections.

Finally, to assess the effect of different values of $\theta_{s,res}$ used as limits for the above probabilities, two additional values of $\theta_{s,res}$ were considered, i.e.: 0.2% and 1.0%. The results are presented in Tables 3 and 4. In the case of $\theta_{s,res}$ equal to 0.2%, the residual drift risk of all the frames is increased as a stricter limit is used. The SC-MRF-CB exhibits the best performance with probabilities of exceedance of $\theta_{s,res}$ equal to 0.2% in 50 years significantly lower than those of the MRF and SC-MRF. In

**Table 3**
Probability of exceedance of $\theta_{s,res}$ equal to 0.2% in 50 years.

| Frame | P[$\theta_{s,res} \geq$ 0.2% in 50 yrs] | | | | | |
|---|---|---|---|---|---|---|
| | Midfault sites | | | End-of-fault sites | | |
| | 5 km | 10 km | 15 km | 5 km | 10 km | 15 km |
| MRF | 51.6% | 37.6% | 28.7% | 52.2% | 38.4% | 29.7% |
| SC-MRF | 28.5% | 17.2% | 11.5% | 29.2% | 17.8% | 12.1% |
| SC-MRF-CB | 17.4% | 9.3% | 5.8% | 18.0% | 9.8% | 6.1% |

**Table 4**
Probability of exceedance of $\theta_{s,res}$ equal to 1.0% in 50 years.

| | $P[\theta_{s,res} \geq 1.0\%$ in 50 yrs] | | | | | |
|---|---|---|---|---|---|---|
| | Midfault sites | | | End-of-fault sites | | |
| Frame | 5 km | 10 km | 15 km | 5 km | 10 km | 15 km |
| MRF | 24.3% | 14.1% | 9.2% | 25.0% | 14.7% | 9.8% |
| SC-MRF | 11.1% | 5.4% | 3.2% | 11.5% | 5.7% | 3.4% |
| SC-MRF-CB | 10.8% | 5.3% | 3.1% | 11.2% | 5.6% | 3.3% |

particular, the SC-MRF-CB has approximately 66%, 75% and 80% reduced probability of exceeding $\theta_{s,res}$ equal to 0.2% in 50 years than that of the conventional MRF for site-to-source distances equal to 5, 10 and 15 km, respectively, at both the midfault and end-of-fault sites. Similarly, The SC-MRF-CB has approximately 39%, 46% and 50% less probability of exceedance of $\theta_{s,res}$ equal to 0.2% in 50 years than that of the SC-MRF for site-to-source distances equal to 5, 10 and 15 km, respectively, at both the midfault and end-of-fault sites.

In the case of $\theta_{s,res}$ equal to 1.0% the residual drift performance of all frames is improved compared to the other two limits. Similar conclusions can be drawn based on the results shown in Table 4. The SC-MRF-CB provides a reduction in the probability of exceedance of $\theta_{s,res}$ equal to 1.0% that ranges between 56% and 66% when compared to the MRF, at both the midfault and end-of-fault sites. This reduction is smaller when the SC-MRF-CB is compared to the SC-MRF and is approximately equal to 2% in all cases. Finally, it is concluded that the SC-MRF-CB is very effective in improving residual drift performance of steel buildings compared to both the MRF and SC-MRF. This improvement is more pronounced in the case of smaller values of $\theta_{s,res}$.

## 10. Conclusions

The potential of SC-MRF-CBs to reduce the residual drift risk of steel buildings in near-fault regions has been assessed. The assessment is based on a prototype steel building designed to use either conventional steel MRFs or SC-MRFs or SC-MRF-CBs. The frames were modelled in OpenSees where material and geometrical non-linearities are considered as well as stiffness and strength degradation. A set of 91 near-fault, pulse-like ground motions with varying pulse periods was used to perform IDA. The probability of exceedance of different residual storey drift limit values was then computed as a function of the ground motion intensity and the period of the velocity pulse. Finally, the results of IDA were combined with NS-PSHA to evaluate and compare the residual drift risk of the three seismic-resistant frames used herein.

Based on the results presented in this paper, the following conclusions can be drawn:

1. The residual drift $S_a(T_1)$ of the frames is affected by the $T_p$ of the near-fault ground motions. It is observed that all the frames are less susceptible in exhibiting residual drift when their fundamental period is very close to the $T_p$ of the excitation.
2. The residual drift risk of all the frames is affected by near-fault directivity. The residual drift fragility curves constructed considering this effect indicate that the SC-MRF-CB exhibits the best residual drift performance.
3. The results show that increased residual drift risk is observed at sites closer to the fault at both midfault and end-of-fault sites.
4. The residual drift risk of all the frames is not as largely affected by the relative position of the site to the fault axis as it is by the distance to the fault. However, slightly larger values of residual drift risk are observed at the end-of-fault sites.
5. The SC-MRF-CB has superior residual drift performance compared to the MRF. A decrease between 56% and 80% in the probability of exceeding three different limit values of $\theta_{s,res}$ in 50 years was achieved by the SC-MRF-CB.
6. The residual drift risk of the SC-MRF-CB is significantly lower compared to that of the SC-MRF. An up to 50% reduction in this risk was achieved by installing the novel steel column base to the SC-MRF.
7. The effectiveness of the novel steel column base in reducing the residual drift risk of steel buildings depends on the limit value of $\theta_{s,res}$. The novel steel column base is more effective in the case of $\theta_{s,res}$ equal to 0.2%.

## CRediT authorship contribution statement

**George S. Kamaris:** Conceptualization, Methodology, Software, Formal analysis, Investigation, Data curation, Visualization, Writing – original draft. **Georgios S. Papavasileiou:** Software, Investigation, Data curation, Writing – review & editing. **Vasileios C. Kamperidis:** Data curation, Investigation, Writing – review & editing. **George Vasdravellis:** Writing – review & editing.

## Declaration of competing interest

The authors declare that they have no known competing financial interests or personal relationships that could have appeared to influence the work reported in this paper.

## References

[1] Iervolino I, Cornell CA. Probability of occurrence of velocity pulses in near-source ground motions. Bull Seismol Soc Am 2008;98(5):2262–77.
[2] Chioccarelli E, Iervolino I. Near-source seismic demand and pulse-like records: a discussion for L'aquila earthquake. Earthq Eng Struct Dynam 2010;39(9):1039–62.
[3] Somerville PG, Smith NF, Graves RW, Abrahamson NA. Modification of empirical strong ground motion attenuation relations to include the amplitude and duration effects of rupture directivity. Seismol Res Lett 1997;68(1):199–222.
[4] Veletsos A, Newmark NM. Effect of inelastic behaviour on response of simple systems to earthquake motions. In: Proc., 2nd world conf. On earthquake engineering, vol. II; 1960. p. 895–912. Tokyo.
[5] Bertero VV, Mahin SA, Herrera RA. Aseismic design implications of near-fault San Fernando earthquake records. Earthq Eng Struct Dynam 1978;6(1):31–42.
[6] Chopra AK, Chintanapakdee C. Comparing response of SDF systems to near-fault and far-fault earthquake motions in the context of spectral regions. Earthq Eng Struct Dynam 2003;30:1769–89.
[7] Mavroeidis GP, Dong G, Papageorgiou AS. Near-fault ground motions and the response of elastic and inelastic,single-degree-of-freedom (SDOF) systems. Earthq Eng Struct Dynam 2004;33:1023–49.
[8] Alavi B, Krawinkler H. Behavior of moment-resisting frame structures subjected to near-fault ground motions. Earthq Eng Struct Dynam 2004;33:687–706.
[9] Makris N, Psychogios T. Dimensional response analysis of yielding structures with first-mode dominated response. Earthq Eng Struct Dynam 2006;35(10):1202–24.
[10] Karavasilis TL, Makris N, Bazeos N, Beskos DE. Dimensional response analysis of multistory regular steel MRF subjected to pulselike earthquake ground motions. J Struct Eng 2010;136(8):921–32.
[11] Champion C, Liel A. The effect of near-fault directivity on building seismic collapse risk. Earthq Eng Struct Dynam 2012;41(10):1391–409.
[12] McCormick J, Aburano H, Ikenaga M, Nakashima M. Permissible residual deformation levels for building structures considering both safety and human elements. In: The 14th world Conference on earthquake Engineering, Beijing, China, October 12-17; 2008.
[13] Ruiz-Garcia J, Miranda E. Residual displacement ratios for assessment of existing structures. Earthq Eng Struct Dynam 2006;35:315–36.
[14] Tzimas AS, Kamaris GS, Karavasilis TL, Galasso C. Collapse risk and residual drift performance of steel buildings using post-tensioned MRFs and viscous dampers in near-fault regions. Bull Earthq Eng 2016;14:1643–62.
[15] EC8. Eurocode 8. Design of structures for earthquake resistance - Part 1: general rules, seismic actions and rules for buildings. 2013.
[16] Ricles JM, Sause R, Garlock MM, Zhao C. Postensioned seismic-resistant connections for steel frames. J Struct Eng 2001;127(2):113–21.
[17] Christopoulos C, Filiatrault A, Uang C-M. Post-tensioned energy dissipating connections for moment resisting steel frames. J Struct Eng 2002;128(9):1111–20.
[18] Vasdravellis G, Karavasilis TL, Uy B. Large-scale experimental validation of steel post-tensioned connections with web hourglass pins. J Struct Eng 2013;139(6):1033–42.
[19] Chou CC, Lai YJ. Post-tensioned self-centering moment connections with beam bottom flange energy dissipators. J Constr Steel Res 2009;65(10–11):1931–41.
[20] Chou C-C, Tsai K-C, Yang W-C. Self-centering steel connections with steel bars and a discontinuous composite slab. Earthq Eng Struct Dynam 2009;38(4):403–22.
[21] Vasdravellis G, Karavasilis TL, Uy B. Finite element models and cyclic behaviour of self-centering post-tensioned connections with web hourglass pins. Eng Struct 2013;52:1–16.

[22] Dimopoulos A, Karavasilis TL, Vasdravellis G, Uy B. Seismic design, modelling and assessment of self-centering steel frames using post-tensioned connections with web hourglass shape pins. Bull Earthq Eng 2013;11(5):1797–816.
[23] Rojas P, Ricles JM, Sause R. Seismic performance of post-tensioned steel moment resisting frames with friction devices. J Struct Eng 2004;131(4):529–40.
[24] Kim HJ, Christopoulos C. Friction damped posttensioned self-centering steel moment-resisting frames. J Struct Eng 2008;134(11):1768–79.
[25] Tsai KC, Chou CC, Lin CL, Chen PC, Jhang SJ. Seismic self-centering steel beam-to-column moment connections using bolted friction devices. Earthq Eng Struct Dynam 2008;37(4):627–45.
[26] Wolski M, Ricles JM, Sause R. Experimental study of a self-centering beam-column connection with bottom flange friction device. J Struct Eng 2009;135(5):479–88.
[27] Garlock M, Sause R, Ricles JM. Behavior and design of posttensioned steel frame systems. J Struct Eng 2007;133(3):389–99.
[28] Kim HJ, Christopoulos C. Seismic design procedure and seismic response of post-tensioned self-centering steel frames. Earthq Eng Struct Dynam 2008;38(3):355–76.
[29] Chou C-C, Chen J-H. Analytical model validation and influence of column bases for seismic responses of steel post-tensioned self-centering MRF systems. Eng Struct 2011;33:2628–43.
[30] Kamperidis VC, Karavasilis TL, Vasdravellis G. Self-centering steel column base with metallic energy dissipation devices. J Constr Steel Res 2018;149:14–30.
[31] Freddi F, Dimopoulos CA, Karavasilis TL. Rocking damage-free steel column base with friction devices: design procedure and numerical evaluation. Earthq Eng Struct Dynam 2017;46:2281–300.
[32] Freddi F, Dimopoulos CA, Karavasilis TL. Experimental evaluation of a rocking damage-free steel column base with friction devices. J Struct Eng 2020;146(10):4020217.
[33] Chi H, Liu J. Seismic behavior of post-tensioned column base for steel self-centering moment resisting frame. J Constr Steel Res 2012;78:117–30.
[34] Wang X-T, Xie C-D, Lin L-H, Li J. Seismic behavior of self-centering concrete-filled square steel tubular (CFST) Column Base. J Constr Steel Res 2019;156:75–85.
[35] Latour M, Rizzano G, Santiago A, Simões da Silva L. Experimental response of a low-yielding, self-centering, rocking column base joint with friction dampers. Soil Dynam Earthq Eng 2019;116:580–92.
[36] Elettore E, Freddi F, Latour M, Rizzano G. Design and analysis of a seismic resilient steel moment resisting frame equipped with damage-free self-centering column bases. J Constr Steel Res 2021;179:106543.
[37] Elettore E, Lettieri A, Freddi F, Latour M, Rizzano G. Performance-based assessment of seismic-resilient steel moment resisting frames equipped with innovative column base connections. Structures 2021;32:1646–64.
[38] Kamperidis VC, Papavasileiou GS, Kamaris GS, Vasdravellis G. Seismic collapse of self-centering steel MRFs with different column base structural properties. J Constr Steel Res 2020;175:106364.
[39] Mazzoni S, McKenna F, Scott M, Fenves G. Open system for earthquake engineering simulation (OpenSees). User command language manual, pacific earthquake engineering research center. Berkeley: University of California; 2006.
[40] Vamvatsikos D, Cornell CA. Incremental dynamic analysis. Earthq Eng Struct Dynam 2002;31(3):491–514.
[41] Vasdravellis G, Karavasilis TL, Uy B. Design rules, experimental evaluation, and fracture models for high-strength and stainless-steel hourglass shape energy dissipation devices. J Struct Eng 2014;140:4014087.
[42] ASTM, ASTM. A416/A416M-05, standard specification for steel strand. West Conshohocken, PA, USA: Uncoated Seven-Wire for Prestressed Concrete; 2005.
[43] Scott MH, Fenves GL. Plastic hinge integration methods for force –based neam-column elements. J Struct Eng 2006;132(2):244–52.
[44] Lignos DG, Krawinkler H. Deterioration modeling of steel components in support of collapse prediction of steel moment frames under earthquake loading. J Struct Eng 2011;137(11):1291–302.
[45] Hamidia M, Filiatrault A, Aref A. Simplified seismic sidesway collapse analysis of frame buildings. Earthq Eng Struct Dynam 2014;43(3):429–48.
[46] Krawinkler H. Shear design of steel frame joints. *Engineering Journal*, AISC 1978;15(2):82–91.
[47] Baker JW. Quantitative classification of near-fault ground motions using wavelet analysis. Bull Seismol Soc Am 2007;97(5):1486–501.
[48] Pacific earthquake engineering research center. NGA Database. http://peer.berkeley.edu/nga/.
[49] FEMA P695. Quantification of building seismic performance factors. ATC-63 Project. USA: Applied Technology Council. CA; 2008.
[50] FEMA-356. Pre-standard and commentary for the seismic rehabilitation of buildings. Washington, D.C: Federal Emergency Management Agency; 2000.
[51] Liel AB, Haselton CB, Deierlein GG, Baker JW. Incorporating modeling uncertainties in the assessment of seismic collapse risk of buildings. Struct Saf 2009;31(2):197–211.
[52] Tothong P, Cornell CA, Baker JW. Explicit directivity-pulse inclusion in probabilistic seismic hazard analysis. Earthq Spectra 2007;23(4):867–91.
[53] Shahi SK, Baker JW. An empirically calibrated framework for including the effects of near fault directivity in probabilistic seismic hazard analysis. Bull Seismol Soc Am 2011;101(2):742–55.
[54] Somerville PG. Magnitude scaling of the near fault rupture directivity pulse. Phys Earth Planet In 2003;137(1):201–12.
[55] Wells DL, Coppersmith KJ. New empirical relationships among magnitude, rupture length, rupture width, rupture area, and surface displacement. Bull Seismol Soc Am 1994;84(4):974–1002.